

# Geophysical Research Letters

## RESEARCH LETTER

10.1029/2021GL093361

### Special Section:

Carbon Weather: Toward the next generation of regional greenhouse gas inversion systems

### Key Points:

- We interpret an ensemble of airborne measurements with the GEOS-Chem model to constrain US fossil fuel and nonfossil carbon monoxide (CO) sources
- Measurements reveal an approximate 30% overestimate of US fossil fuel CO emissions in the National Emissions Inventory
- During summer regional fossil fuel sources account for just 9%–16% of total boundary layer CO over eastern North America

### Supporting Information:

Supporting Information may be found in the online version of this article.

### Correspondence to:

D. B. Millet,  
[dbm@umn.edu](mailto:dbm@umn.edu)
















### Citation:

Gonzalez, A., Millet, D. B., Yu, X., Wells, K. C., Griffis, T. J., Baier, B. C., et al. (2021). Fossil versus nonfossil CO sources in the US: New airborne constraints from ACT-America and GEM. *Geophysical Research Letters*, 48, e2021GL093361. <https://doi.org/10.1029/2021GL093361>

Received 16 MAR 2021

Accepted 15 MAY 2021

## Fossil Versus Nonfossil CO Sources in the US: New Airborne Constraints From ACT-America and GEM

Andres Gonzalez<sup>1</sup> , Dylan B. Millet<sup>1</sup> , Xueying Yu<sup>1</sup> , Kelley C. Wells<sup>1</sup> , Timothy J. Griffis<sup>1</sup> , Bianca C. Baier<sup>2,3</sup> , Patrick C. Campbell<sup>4,5,6</sup> , Yonghoon Choi<sup>7</sup> , Joshua P. DiGangi<sup>7</sup> , Alexander Gvakharia<sup>8</sup> , Hannah S. Halliday<sup>7</sup> , Eric A. Kort<sup>8</sup> , Kathryn McKain<sup>2,3</sup> , John B. Nowak<sup>7</sup> , and Genevieve Plant<sup>8</sup> 

<sup>1</sup>Department of Soil, Water, and Climate, University of Minnesota, Saint Paul, MN, USA, <sup>2</sup>Cooperative Institute for Research in Environmental Sciences (CIRES), University of Colorado, Boulder, CO, USA, <sup>3</sup>Global Monitoring Laboratory, National Oceanic and Atmospheric Administration, Boulder, CO, USA, <sup>4</sup>Center for Spatial Information Science and Systems, George Mason University, Fairfax, VA, USA, <sup>5</sup>Cooperative Institute for Satellite Earth System Studies (CISESS), College Park, MD, USA, <sup>6</sup>Air Resources Laboratory, National Oceanic and Atmospheric Administration, College Park, MD, USA, <sup>7</sup>NASA Langley Research Center, Hampton, VA, USA, <sup>8</sup>Department of Climate and Space Sciences and Engineering, University of Michigan, Ann Arbor, MI, USA

**Abstract** Carbon monoxide (CO) is an ozone precursor, oxidant sink, and widely used pollution tracer. The importance of anthropogenic versus other CO sources in the US is uncertain. Here, we interpret extensive airborne measurements with an atmospheric model to constrain US fossil and nonfossil CO sources. Measurements reveal a low bias in the simulated CO background and a 30% overestimate of US fossil CO emissions in the 2016 National Emissions Inventory. After optimization we apply the model for source partitioning. During summer, regional fossil sources account for just 9%–16% of the sampled boundary layer CO, and 32%–38% of the North American enhancement—complicating use of CO as a fossil fuel tracer. The remainder predominantly reflects biogenic hydrocarbon oxidation plus fires. Fossil sources account for less domain-wide spatial variability at this time than nonfossil and background contributions. The regional fossil contribution rises in other seasons, and drives ambient variability downwind of urban areas.

**Plain Language Summary** Carbon monoxide (CO) is an air pollutant emitted from fossil fuel combustion and from forest and agricultural fires. CO is also produced in the atmosphere through the oxidation of hydrocarbons from both natural and human-caused sources. US fossil fuel CO emissions have been declining in recent years, and their current importance relative to other regional sources is uncertain. Here, we interpreted a large group of aircraft-based CO measurements with a high-resolution atmospheric model to better quantify US fossil and nonfossil fuel CO sources over the eastern half of the US. We find that US fossil fuel CO emissions in the 2016 National Emissions Inventory are overestimated by ~30%. Furthermore, during summer regional fossil fuel sources account for only a small fraction of the CO over North America compared to the background concentrations already present in air entering North America, and compared to the regional source from natural hydrocarbon oxidation. This complicates the use of CO as a tracer for estimating fossil fuel sources of other pollutants such as carbon dioxide.

## 1. Introduction

Carbon monoxide (CO) is the largest sink of atmospheric hydroxyl (OH) radicals (Müller et al., 2018) and a major tropospheric ozone precursor (Hu et al., 2017). It is emitted from fossil fuel and biomass combustion and is also indirectly produced from the oxidation of methane and non-methane volatile organic compounds (VOCs). CO removal occurs mainly via reaction with OH, forming atmospheric carbon dioxide (CO<sub>2</sub>) at an annual rate equivalent to ~10% of the global fossil fuel source (Duncan et al., 2007; Friedlingstein et al., 2019). As a result of its oxidative effects and their feedbacks, CO has a 100-year global warming potential ~5 times that of CO<sub>2</sub> per unit mass (Shindell et al., 2009).

According to the National Emissions Inventory Collaborative (NEIC) Emissions Modeling Platform, based on the US Environmental Protection Agency (EPA) National Emissions Inventory (NEI), US CO emissions totaled ~55 Tg in 2016, with fossil fuel and biomass burning emissions accounting for 41 Tg and 14 Tg,

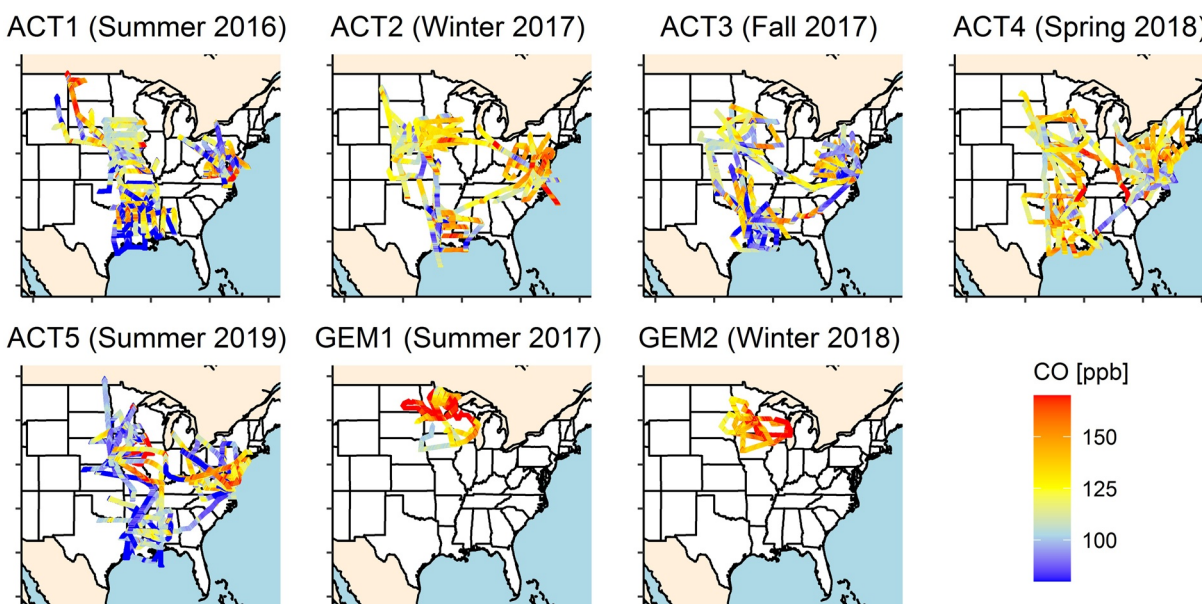


**Figure 1.** Atmospheric Carbon and Transport (ACT)-America and Greenhouse Emissions in the Midwest (GEM) flight-tracks colored by observed carbon monoxide (CO) mixing ratios.

respectively (NEIC, 2019). Fossil fuel sources in the inventory are predominantly mobile (on-road: 18 Tg; non-road: 10 Tg) and in the case of on-road emissions, mainly (90%) due to non-diesel light-duty vehicles. Gasoline combustion similarly accounts for the majority (80%) of the estimated non-road mobile source (NEI, 2014). Annual fossil fuel CO emissions in the NEI decreased by ~50 Tg/year from 2000 to 2016, driven by a nearly 70% drop in the estimated mobile source (EPA, 2019).

CO has traditionally been used as a fossil fuel tracer to diagnose anthropogenic sources of CO<sub>2</sub> and other species (e.g., Cheng et al., 2018; Halliday et al., 2019; Nathan et al., 2018; Super et al., 2017). In the US, however, the dramatic decline in transportation-related emissions (EPA, 2019; Gaubert et al., 2017; Parrish, 2006) means that nonfossil fuel CO sources are increasingly important. For example, Hudman et al. (2008) estimated that VOC oxidation (predominantly from biogenic precursors) was a 2-fold larger CO source than direct combustion emissions over the US during summer 2004. Furthermore, previous NEI versions have been shown to overestimate US anthropogenic CO emissions by as much as 60% (Brioude et al., 2011, 2013; Fujita et al., 2012; Hudman et al., 2008; Kim et al., 2013; Müller et al., 2018; Plant et al., 2019; Salmon et al., 2018), so the nonfossil fuel CO fraction may be even greater than suggested by current inventories.

Together, the large recent emission trends and demonstrated inventory biases imply significant uncertainty in the current CO budget over North America. Two airborne measurement campaigns conducted from 2016 to 2019 with widespread, multi-seasonal coverage over the eastern half of the US provide new constraints for addressing this issue: The Atmospheric Carbon and Transport (ACT, 2019)-America mission, with five dual-aircraft deployments across three US regions (Davis et al., 2021), and the Greenhouse Emissions in the Midwest (GEM) mission with three deployments across the US Upper Midwest (Yu et al., 2020; 2021). Here, we employ the GEOS-Chem chemical transport model (CTM) to interpret these datasets in terms of their implications for fossil fuel versus nonfossil and primary versus secondary CO sources over the US.

## 2. Methods

### 2.1. Aircraft Measurements

Figure 1 shows flight-tracks for the ACT-America and GEM airborne deployments used here. ACT-America took place during summer 2016 (ACT1; see Table S1), winter 2017 (ACT2), fall 2017 (ACT3), spring 2018 (ACT4), and summer 2019 (ACT5) (Davis et al., 2018, 2021). Each deployment featured measurements aboard two aircraft (C-130 Hercules: 487 flight hours; Beechcraft B200 King Air: 513 flight hours) across

the US Midwest, Northeast, and South. Sampling altitudes ranged from 0.1 to 8.7 km above ground level (AGL); only data below 8 km AGL are employed here. Airborne CO measurements were also performed for the first two GEM campaigns over the US Upper Midwest during summer 2017 (GEM1) and winter 2018 (GEM2). Measurements took place on a Mooney aircraft (76 flight hours) from 0.1 to 2.2 km AGL (Yu et al., 2020, 2021). We employ data from ACT1 to ACT4 for CO source estimation and reserve ACT5, GEM1, and GEM2 for independent evaluation of the results.

ACT-America CO dry-air mole fraction measurements used here were performed in-situ by wavelength-scanned cavity ring-down spectroscopy (CRDS; Picarro G2401-m) with  $\pm 5$  ppb estimated uncertainty (DiGangi et al., 2021; Wei et al., 2021). Additional CO measurements were obtained during ACT-America via air samples collected on-board both aircraft with Programmable Flask Packages (PFP) (Baier et al., 2020; Davis et al., 2018; Wei et al., 2021). An intercomparison of the C-130-H and B-200 Picarro datasets using the PFP observations as transfer standard shows no significant difference (Figure S1) and we treat them here as a single statistical ensemble. GEM CO measurements were performed by continuous-wave tunable infrared laser absorption spectrometry (Aerodyne CW-TILDAS) with  $\pm 1$  ppb estimated uncertainty (Gvakharia et al., 2018; Millet et al., 2019). In-situ measurements for ACT and GEM were made at 0.4 Hz and we use 1-min averaged data in analyses that follow.

We also employ airborne CO measurement over the remote Pacific from the Atmospheric Tomography Mission (ATom) (Wofsy et al., 2018) to evaluate and adjust the chemical boundary conditions used in the nested GEOS-Chem simulations (Section 2.2). ATom featured pole-to-pole sampling from 0.2 to 12 km altitude during four separate deployments; CO measurements used here were collected using the NOAA Picarro instrument with estimated  $\pm 3.6$  ppb uncertainty (Chen et al., 2013). ATom1 (Northern Hemisphere summer 2016), ATom2 (winter 2017), ATom3 (fall 2017), and ATom4 (spring 2018) overlap temporally with ACT1–ACT4, respectively, and are applied for correction accordingly. ATom1 data is further used for ACT5 and GEM1 background correction, and ATom2 data for GEM2 background correction, given their matching seasonal coverage. Correction procedures are explained below. All data sets are calibrated on the WMO X2014A scale.

## 2.2. GEOS-Chem Simulations

We interpret the above airborne datasets using a GEOS-Chem (v12.6.3; doi:10.5281/zenodo.3552959) simulation nested at  $0.25^\circ \times 0.3125^\circ$  (latitude  $\times$  longitude) resolution over North America ( $60^\circ\text{W}$ – $130^\circ\text{W}$ ,  $9.75^\circ\text{N}$ – $60^\circ\text{N}$ ) with 47 vertical layers (Figure S2). Model runs are driven by GEOS-FP meteorological data from NASA GMAO (Lucchesi, 2013), and employ timesteps of 10-min (transport, convection) and 20-min (emissions, chemistry). A 1-month nested spinup is used for initialization.

Chemical boundary conditions (3-h) for the nested model domain are obtained from global simulations at  $2^\circ \times 2.5^\circ$  and bias-corrected using a latitude-dependent (and altitude-invariant) fit of model-measurement 0.1 quantile differences ( $6^\circ$  latitude bins from  $66^\circ\text{S}$  to  $54^\circ\text{N}$ ) along the ATom flight-tracks over the remote Pacific (Figure S3). As described later, we also perform a sensitivity analysis without this boundary condition correction as one test of our results.

We use tagged tracers (Fisher et al., 2017) to track contributions to ambient CO from direct and indirect sources within the North American domain shown in Figure S2 and from the chemical boundary conditions ( $\text{CO}_{bc}$ ). Tagged direct sources include US on-road mobile emissions ( $\text{CO}_{usrd}$ ), US non-road mobile emissions ( $\text{CO}_{usnr}$ ), other US anthropogenic sources ( $\text{CO}_{usot}$ ; for example, from power generation, industrial and manufacturing activities, and waste processing), non-US anthropogenic emissions ( $\text{CO}_{camx}$ ; from Canada and Mexico) and wildfires plus agricultural burning ( $\text{CO}_{bb}$ ). We separately track secondary CO ( $\text{CO}_{prod}$ ) from the oxidation of biogenic VOCs ( $\text{CO}_{prod\_bio}$ ), anthropogenic VOCs ( $\text{CO}_{prod\_anth}$ ), and other precursors ( $\text{CO}_{prod\_oth}$ ; methane plus pyrogenic VOCs) occurring within the North American domain. CO production rates are computed using archived fields from global full-chemistry simulations at  $2^\circ \times 2.5^\circ$ ; secondary contributions from biogenic and anthropogenic VOCs are derived from runs with the corresponding emissions perturbed by 10%. Photochemical removal is applied to each of the tagged tracers using offline OH fields (GEOS-Chem v5-07-08); the simulation is thus linear in CO.

Global anthropogenic emissions in the model are from the Community Emissions Data System (Hoesly et al., 2018) overwritten for the US by the 2016 EPA NEI (NEIC2016v1; NEIC, 2019) and for Canada by the Air Pollutant Emission Inventory (APEI, 2020). Biogenic emissions are from the Model of Emissions of Gases and Aerosols from Nature (MEGANv2.1) implemented as described by Hu et al. (2015), and biomass burning emissions use the Quick-Fire Emissions Data Set (Koster et al., 2015). The above CO emission estimates and production rates contain significant uncertainties and the following analyses optimize both on the basis of the ACT-America airborne data. All model-measurement comparisons employ the model plane-flight diagnostic to sample the model output along the aircraft flight-tracks at the time of measurement.

### 3. Results

#### 3.1. Measured Versus Predicted CO Over the Eastern and Central US

Figures 2a–2g shows the mean vertical CO profiles measured during ACT1–ACT5 and GEM1–GEM2. Average concentrations during the ACT-America flights peak in the planetary boundary layer (PBL; defined here as  $z < 2$  km) at ~120–125 ppb during summer and fall and at ~140 ppb during spring and winter. Concentrations during GEM (which sampled farther north and predominantly within the PBL) are slightly higher. Aloft, we see free tropospheric ( $z > 4$  km) concentrations ranging seasonally between ~80–90 ppb (summer) and ~100–110 ppb (winter).

Also shown in Figures 2a–2g are the CO mixing ratios simulated by GEOS-Chem along the flight-tracks at the time of measurement, with the corresponding tagged-tracer source contributions. The base-case simulation successfully captures the relative vertical distribution of CO, but underestimates its abundance in all seasons except fall (ACT3). The magnitude of this low bias during spring, summer, and winter ranges from 9 ppb (averaged below 2 km) during spring for ACT4 to 48 ppb during summer for GEM1.

Transport from outside North America makes the largest contribution to ambient CO over the eastern half of the US in the GEOS-Chem base-case simulation (Figures 2a–2g). This background varies little with altitude and changes seasonally in concert with the CO lifetime, from ~50 ppb in summer (for ACT1 and ACT5) to ~100 ppb in winter (for ACT2 and GEM2). We see from Figure 2 that the background contribution dominates total CO in the free troposphere (71%–96% above 4 km, lowest in summer). At lower altitudes, regional CO sources play a larger role; nevertheless, the CO background still represents 55% (summer)–78% (winter) of the total averaged model abundance below 2 km.

Figures 2h–2n shows the base-case model partitioning of North American CO enhancements (i.e., excluding  $\text{CO}_{bc}$ , which is already present in air entering North America) during ACT-America and GEM. The regional secondary source is further partitioned into biogenic, anthropogenic, and other (methane + pyrogenic VOC) contributions. Secondary production accounts for a significant fraction of the predicted North American CO source, particularly during summer when, in the case of ACT1 and ACT5, it mainly arises from biogenic VOC oxidation. Primary emissions mainly reflect US anthropogenic sources (in turn dominated by on-road and off-road mobile emissions). GEM1, over the Upper Midwest, featured a larger contribution from biomass burning.

#### 3.2. CO Source Optimization

We next apply the base-case tagged tracer simulations discussed above to develop improved US CO source estimates based on the ACT-America observations. The optimization is performed separately for ACT1–ACT4 and consists of two steps. First, since background CO dominates the total free tropospheric abundance (Figure 2), we attribute the prior model bias aloft accordingly and correct the simulated  $\text{CO}_{bc}$  based on the mean  $>4$  km model-measurement differences for each campaign. Given the vertical uniformity of  $\text{CO}_{bc}$  this correction is applied throughout the column and ranges from a factor of 1.0 during fall to 1.5 during summer. This adjustment (along with the ATom-based adjustment described earlier) also implicitly corrects for the effects of a potential model OH bias on the simulated CO.

Second, after subtracting this corrected background we derive top-down adjustments on regional CO sources by regressing the model tagged tracers against the observed above-background enhancements below 2 km AGL. Selected tracers are grouped for optimization to avoid multicollinearity and based on their



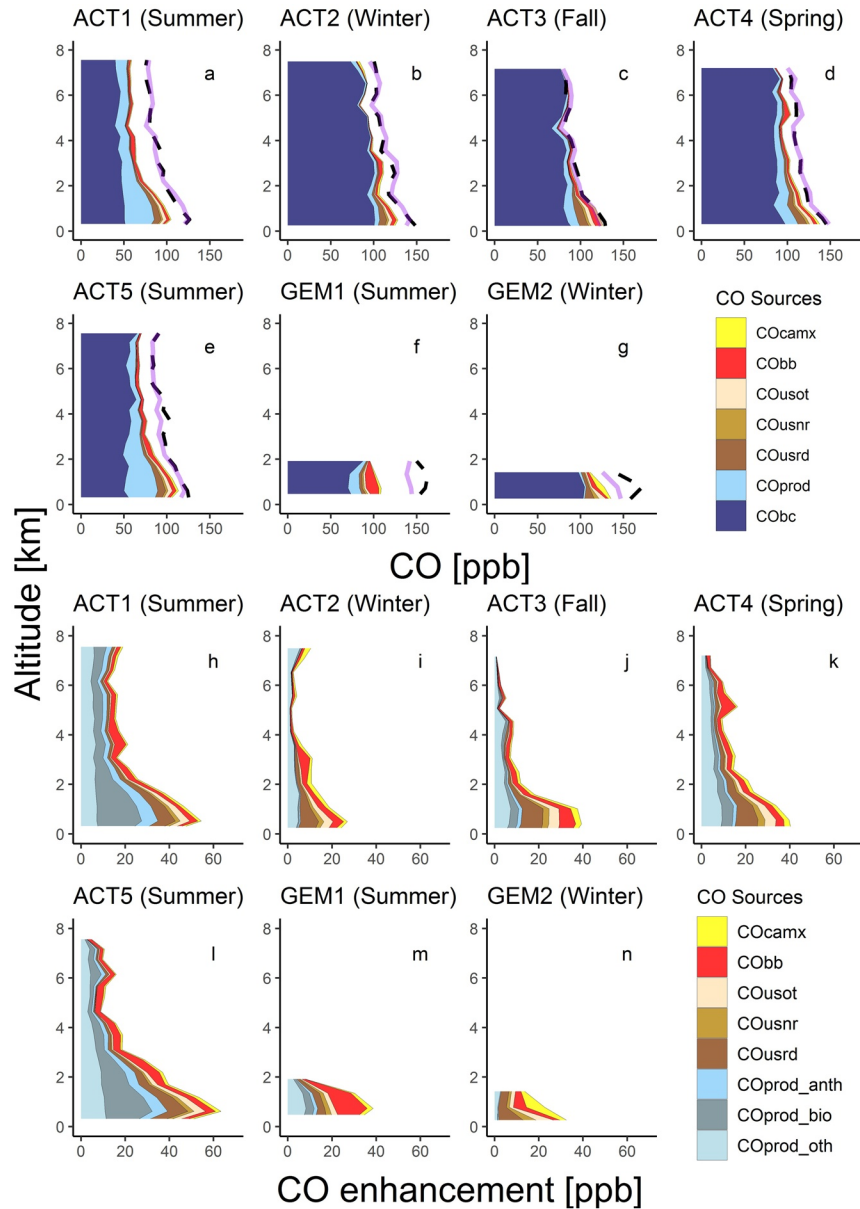


**Figure 2.** Mean carbon monoxide (CO) profiles during Atmospheric Carbon and Transport (ACT)-America and Greenhouse Emissions in the Midwest (GEM). Panels (a–g) compare observed CO mixing ratios (black dashed lines) with those predicted by the prior GEOS-Chem simulation (stacked color plots). Pink lines show simulated CO concentrations after source optimization. Panels (h–n) show the above-background source contributions based on the prior GEOS-Chem simulation.  $CO_{usrd}$ ,  $CO_{usnr}$ ,  $CO_{usot}$ : Anthropogenic CO from US on-road, non-road, and other sources.  $CO_{camx}$ : Anthropogenic CO emitted in Canada + Mexico.  $CO_{bb}$ : CO from North American biomass burning.  $CO_{prod}$ : CO photochemically produced over North America from the oxidation of biogenic volatile organic compounds (VOCs) ( $CO_{prod_{bio}}$ ), anthropogenic VOCs ( $CO_{prod_{anth}}$ ), and methane + biomass burning VOCs ( $CO_{prod_{oth}}$ ).  $CO_{bc}$ : CO transported from outside North America.

relative abundance. During summer we thus optimize (a) direct CO emissions from US onroad, non-road mobile, and other anthropogenic sources ( $CO_{usnei} = CO_{usrd} + CO_{usnr} + CO_{usot}$ ) and (b) regional secondary CO production from biogenic and anthropogenic VOCs ( $CO_{prod_{voc}} = CO_{prod_{bio}} + CO_{prod_{anth}}$ ) as single variables based on the high cross-correlation ( $R = 0.92$ – $0.98$ ) among the grouped tracers. Other secondary production ( $CO_{prod_{oth}}$ ) is not optimized as it is primarily from methane and implicitly corrected by the preceding background adjustment. CO sources from Canada and Mexico and from biomass burning each

**Table 1**  
Seasonal CO Source Optimization<sup>a</sup>

	CO <sub>usnei</sub>		CO <sub>prod_voc</sub>		Intercept	VIF <sup>b</sup>	Mean bias <sup>c</sup> (ppb)		RMSE <sup>d</sup> (ppb)		R	
	Scale factor	Mean (ppb)	Scale factor	Mean (ppb)			Prior	Post	Prior	Post	Prior	Post
ACT1 (summer)	0.66 ± 0.05	13.2	0.91 ± 0.03	25.4	−0.2 ± 0.3	3.1	−17.6	0.2	26.4	16.5	0.75	0.81
ACT2 (winter)	0.79 ± 0.03	12.8			1.8 ± 0.3		−14.8	−1.7	21.4	15.5	0.69	0.69
ACT3 (fall)	0.69 ± 0.03	16.8			5.5 ± 0.5		−2.5	−5.5	13.4	14.2	0.79	0.75
ACT4 (spring)	0.74 ± 0.02	16.9			−2.7 ± 0.4		−8.8	2.6	18.1	17.0	0.65	0.62

Note. ACT1–ACT4 refer to the first four Atmospheric Carbon and Transport (ACT)-America campaigns.

<sup>a</sup>Stated uncertainties reflect 95% confidence intervals computed through bootstrap resampling. <sup>b</sup>Variance inflation factor. <sup>c</sup>Mean of simulated minus observed values. <sup>d</sup>Root mean square error.

Abbreviation: CO: carbon monoxide.

make up <18% of the above-background model abundance during ACT1–4 and are likewise not optimized. During other seasons the same procedure is used but without optimizing CO<sub>prod\_voc</sub> as it then accounts for <16% of the mean above-background enhancements. A sensitivity test described later explores how the choice of tracer groups for optimization affects our results.

In this way, we obtain seasonal top-down correction factors for the NEIC2016v1 US anthropogenic CO emissions, along with a top-down correction to the regional secondary source from biogenic + anthropogenic VOCs during summer. Results shown in Table 1 are consistent across the seasonal ACT-America campaigns in revealing a moderate NEI overestimate of US anthropogenic CO emissions, with coefficients ranging from 0.66 ± 0.05 to 0.79 ± 0.03 (here and below, stated uncertainties reflect bootstrapped 95% confidence intervals). We find that secondary CO production from regional VOC oxidation is well-represented in the model, with a derived scale factor of 0.91 ± 0.03.

Figure 2 and Table 1 show that the optimization successfully minimizes the prior model bias, and either improves or maintains the prior model:measurement correlation. An exception is ACT3, where the prior simulation was already essentially unbiased (<3 ppb) with high correlation. However, the posterior fit quality here is still comparable to that obtained in other seasons. In the following section, we apply a series of statistical and sensitivity analyses and independent data comparisons to further test the representativeness and robustness of these results.

### 3.3. Uncertainty Analysis

The bootstrapped uncertainty estimates in Table 1 provide a first evaluation of the optimization results, showing that the individual scaling coefficients derived from ACT1 through ACT4 are each statistically robust. The similar findings across ACT1–ACT4 provide a second piece of supporting evidence, as the deployments represent four separate data sets and independent source derivations that all lead to consistent results—despite seasonally varying CO sources, background contributions, and OH. Third, we see from Figure 2 and Table S2 that the CO source optimization (derived from ACT1–ACT4 data) strongly improves model performance versus independent airborne data from ACT5, GEM1, and GEM2, which were not employed in the optimization.

As a fourth test, we perform the CO source optimization separately for the two ACT-America aircraft. Table S3 shows that we arrive at the same conclusions when analyzing the B-200 and C-130 observations independently as opposed to treating them as a combined data set. Specifically, we infer an NEI overestimate of US anthropogenic CO emissions in both cases, with derived scale factors spanning 0.54–0.87 (sensitivity tests) versus 0.66–0.79 (base analysis). The modest adjustment to the modeled secondary CO source from regional biogenic and anthropogenic VOCs is likewise independently supported by both airborne data sets (scale factors of 0.74–0.96 vs. 0.91 in the base-case).

A fifth evaluation repeats the base-case optimization with alternate boundary conditions (CO<sub>bc</sub>) for the nested model domain—that is, employing the native model output for this purpose and omitting the

ATom-based background adjustment (Section 2.2; Figure S3). Results in Table S4 show that scale factors derived in this way are statistically consistent with the base-case analysis. For a sixth and final test, we modify the tracer groupings used for optimization and instead derive ACT1–ACT4 scale factors for (a)  $\text{CO}_{\text{usnei}}$  and (b) the sum of all other regional source tracers. Results shown in Table S5 are again consistent with the base-case findings, with a slightly wider range for the  $\text{CO}_{\text{usnei}}$  scale factor (0.58–0.85) and a modestly degraded observational fit.

Overall, the above uncertainty tests all support our core findings, and we proceed to interpret the optimized results in terms of their implications for fossil fuel versus nonfossil, and primary versus secondary, CO sources over the US.

### 3.4. Optimized CO Source Contributions

Figures 3a–3g shows the optimized primary and secondary North American contributions to ambient CO as sampled during ACT-America and GEM. We find that secondary production (mainly from biogenic VOCs) is the dominant summertime North American CO source for air masses sampled by ACT-America, accounting for ~70% of the total PBL enhancement. Secondary production is also significant at other times (e.g., 26%–45% of the PBL enhancement during the fall, winter, and spring ACT-America campaigns) but then mainly reflects regional methane oxidation along with pyrogenic VOC oxidation. To the north, the importance of secondary CO over the Upper Midwest during GEM is significantly less (~7%–40%)—reflecting lower biogenic VOC emissions and slower regional photochemistry. In total, photochemical CO sources contribute between 2 ppb (winter; GEM2) and 31 ppb (summer; ACT5) to the average sampled PBL enhancements, versus 13–25 ppb from primary emissions.

In Figures 3h–3n, we further partition the optimized CO abundance into fossil fuel versus nonfossil contributions. Here, fossil fuel sources include primary emissions plus secondary production from anthropogenic VOC, while nonfossil fuel sources include biogenic VOC oxidation plus biomass burning CO emissions. The remainder is from the oxidation of methane and of fire-derived VOCs. Results show that fossil fuel sources account for just 32%–38% of the North American PBL CO enhancements sampled by ACT-America and GEM during summer, increasing to 48%–49% during spring/fall and 57%–84% during winter.

The findings above reveal the complications of using CO as an anthropogenic tracer, particularly during summer—as fossil fuel sources account for just 9%–16% of the total PBL abundance, and 32%–38% of the North American enhancement, during this season. However, for many applications (e.g., applying species:species correlations for source partitioning), source impacts on tracer variability can be more important than their absolute magnitude. For example, one might expect the secondary CO source to be relatively diffuse and that direct anthropogenic emissions would be a more important driver of ambient CO variability over the US.

To explore this expectation, Figures S4–S5 show the CO standard deviation by source category (based on the optimized GEOS-Chem simulation) for each airborne campaign in its entirety. In the summertime PBL sampled by ACT-America and GEM, the CO variability due to North American (primary + secondary) fossil fuel sources is substantially smaller (7–10 ppb) than that associated with background (15–21 ppb) and regional nonfossil fuel (11–15 ppb) contributions. In other seasons, regional fossil fuel emissions drive as much or more of the CO variability than nonfossil sources, but (except in the case of GEM) this variability is still smaller than that associated with the CO background.

The characterization above, treating each ACT-America and GEM campaign as a single statistical data set, mainly describes spatial patterns of CO variability across the eastern half of the US as a whole. If we instead apply the optimized model to map the drivers of temporal CO variability (Figures S6–S10), we observe in all seasons a dominant role for fossil fuel emissions in and downwind of most urbanized areas. A similar finding applies for fires in specific affected regions. Temporal variability associated with secondary CO, manifesting most strongly in summer, is relatively low over much of the US Southeast where precursor VOC emissions are highest but is elevated around the periphery of this region (e.g., Figures S6, S11, and S16). We attribute this to transport-driven effects at the edges of a large and diffuse source region (Figures S11–S15). In other seasons, temporal variability associated with secondary CO is small, with fossil fuel emissions, biomass burning, and background CO playing more important roles (Figures S7–S9).

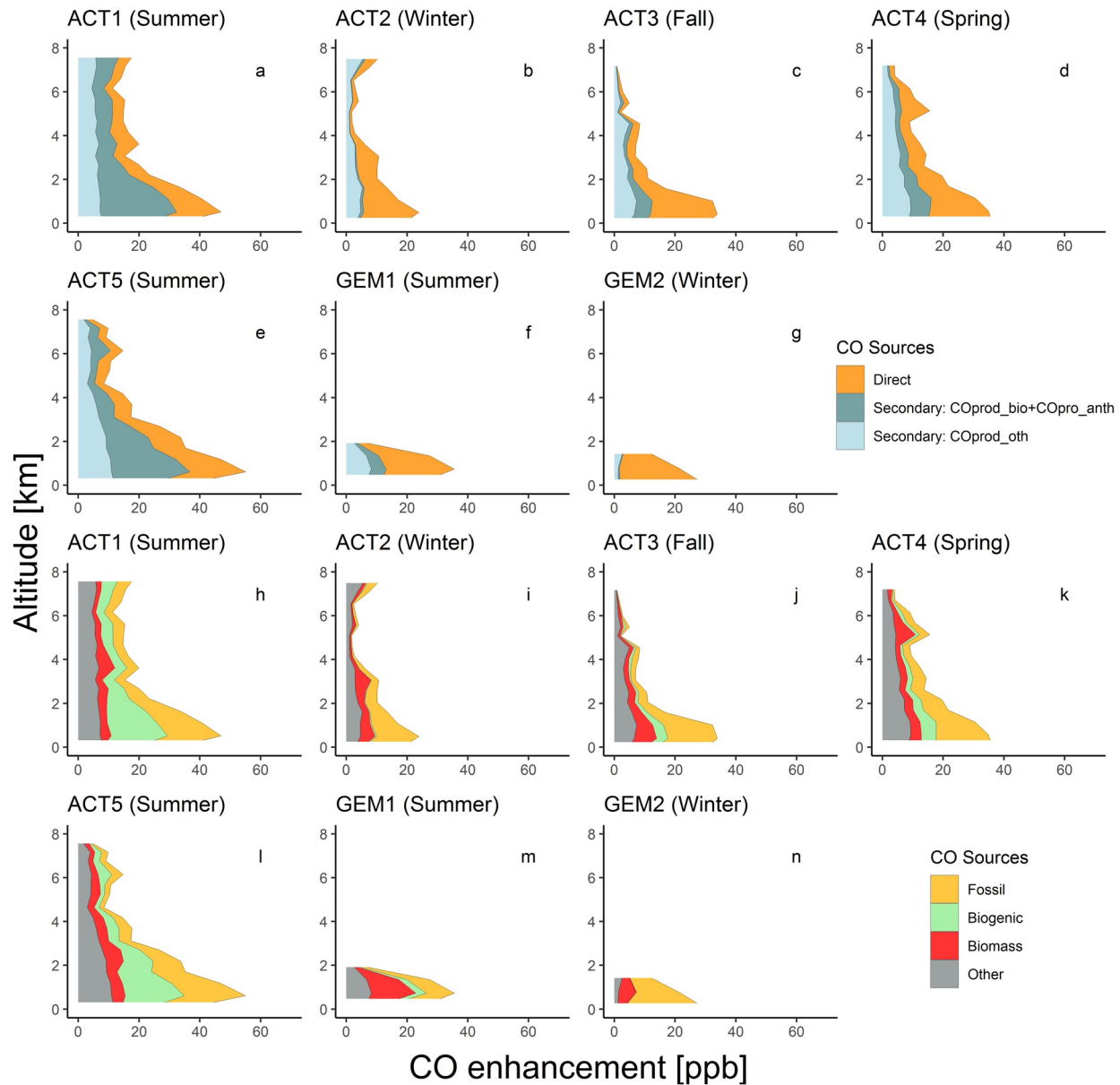


**Figure 3.** Observationally constrained carbon monoxide (CO) source attribution over the eastern US. Plotted are the mean above-background CO profiles from the optimized GEOS-Chem simulation along the aircraft flight-tracks. Panels (a–g) partition the regional CO enhancements into direct and secondary components. Direct sources include: Anthropogenic CO from US on-road ( $CO_{usrd}$ ), non-road ( $CO_{usnr}$ ), and other sources ( $CO_{usor}$ ), anthropogenic CO emitted in Canada + Mexico ( $CO_{camx}$ ), and biomass burning CO ( $CO_{bb}$ ). Secondary sources ( $CO_{prod}$ ) include oxidation of biogenic + anthropogenic VOCs ( $CO_{prod\_bio} + CO_{prod\_anth}$ ) and of methane + biomass burning VOCs ( $CO_{prod\_oth}$ ). Panels (h–n) partition the regional CO enhancements into fossil fuel (direct + secondary), biogenic (exclusively secondary), biomass burning (direct), and other (mainly methane oxidation, plus secondary biomass burning) contributions.

#### 4. Conclusions

We applied measurements from 13 airborne campaigns to develop new constraints on CO sources over the central and eastern US. Data were collected over 1,000 flight hours across all seasons, representing the densest airborne data set yet for CO source quantification over North America. Campaign-average PBL (<2 km) mixing ratios ranged from 121 (summer) to 158 ppb (winter). Interpreting this data set with a high-resolution version of the GEOS-Chem CTM driven by the US EPA's NEIC2016v1 inventory, we find that the model accurately captures the observed CO vertical profile shape but underestimates its abundance (by 9–48 ppb) in all seasons except fall. This disparity partly reflects a bias in the model CO background,



and after correction we infer an NEI overestimate of fossil fuel CO emissions, with a derived top-down adjustment factor of 0.72 (0.54–0.87; best estimate and uncertainty range across all sensitivity tests and seasons). For comparison, the US EPA estimates that national fossil fuel CO emissions decreased by 8% from 2016 to 2019 (EPA, 2019). Our top-down estimate for the secondary CO source from North American VOC emissions agrees well with the prior model value, with a derived scale factor of 0.91 (0.74–0.96). If the above comparisons are nationally representative, the implied US fossil fuel CO source for 2016–2019 was 29 (22–36) Tg/y, compared to the prior NEIC2016v1 estimate of 41 Tg/y (for 2016).

After optimizing the model based on the airborne constraints, we find that the CO background represents on average 55%–78% of the PBL CO sampled during the aircraft campaigns. During summer, North American fossil fuel sources account for only 9%–16% of the sampled PBL CO, and 32%–38% of the enhancements associated with regional sources. Nonfossil sources from biogenic VOC oxidation and fires account for 40%–45% of the above-background enhancements at this time, with the remainder mainly from regional methane oxidation. In other seasons, however, fossil fuel emissions are the largest regional source of CO.

Application of CO as a fossil fuel tracer is challenged by the fact that, during the growing season, such sources account for only a modest fraction of the CO burden and its spatial variability across the US. However, in and near most urbanized regions the temporal variability in CO is still dominated by fossil fuel sources. The number of locations where this remains the case will likely diminish, as US fossil fuel CO emissions are expected to continue declining with future vehicle emission regulations, advanced emission after-treatment technologies, and fleet electrification (Nopmongkol et al., 2017; Winkler et al., 2018).

## Data Availability Statement

The ACT-America, GEM, and ATom data sets are publicly available at <https://doi.org/10.3334/ORN-LDAAC/1593>, <https://doi.org/10.13020/f50r-zh70>, and <https://doi.org/10.3334/ORN-LDAAC/1581>. GEOS-Chem model code is publicly available at <http://www.geos-chem.org>. Tagged CO model code and boundary conditions used here are available at <https://doi.org/10.13020/p2ze-1y93>.

## Acknowledgments

This work was supported by NASA (Grant #NNX17AK18G) and the Minnesota Supercomputing Institute. This work was also supported in part by NSF Grant #1650682 (E. A. Kort, A. Gonzalez, and G. Plant) and by NASA Grants #NNX15AJ06G (B. C. Baier), #NNX15AJ23G (ATom campaign), and #80NSSC18K1393 (X. Yu). The authors thank K. Davis, Z. Barkley, and the entire ACT-America team for their contributions.

## References

- ACT (Atmospheric Carbon and Transport)-America (2019). *ACT-America: L3 merged in situ atmospheric trace gases and flask data, eastern USA*. ORNL DAAC. <https://doi.org/10.3334/ORN-LDAAC/1593>
- APEI (2020). *Canada's air pollutant emissions inventory*. Retrieved from <https://open.canada.ca/data/en/dataset/falc88a8-bf78-4fcb-9c1e-2a5534b92131>
- Baier, B. C., Sweeney, C., Choi, Y., Davis, K. J., DiGangi, J. P., Feng, S., et al. (2020). Multispecies assessment of factors influencing regional CO<sub>2</sub> and CH<sub>4</sub> enhancements during the winter 2017 ACT-America campaign. *Journal of Geophysical Research: Atmospheres*, 125, e2019JD031339. <https://doi.org/10.1029/2019JD031339>
- Brioude, J., Angevine, W. M., Ahmadov, R., Kim, S. W., Evan, S., McKeen, S. A., et al. (2013). Top-down estimate of surface flux in the Los Angeles basin using a mesoscale inverse modeling technique: Assessing anthropogenic emissions of CO, NO<sub>x</sub> and CO<sub>2</sub> and their impacts. *Atmospheric Chemistry and Physics*, 13(7), 3661–3677. <https://doi.org/10.5194/acp-13-3661-2013>
- Brioude, J., Kim, S.-W., Angevine, W. M., Frost, G. J., Lee, S.-H., McKeen, S. A., et al. (2011). Top-down estimate of anthropogenic emission inventories and their interannual variability in Houston using a mesoscale inverse modeling technique. *Journal of Geophysical Research: Atmospheres*, 116, D20305. <https://doi.org/10.1029/2011jd016215>
- Cheng, Y., Wang, Y., Zhang, Y., Crawford, J. H., Diskin, G. S., Weinheimer, A. J., & Fried, A. (2018). Estimator of surface ozone using formaldehyde and carbon monoxide concentrations over the eastern United States in summer. *Journal of Geophysical Research: Atmospheres*, 123(14), 7642–7655. <https://doi.org/10.1029/2018JD028452>
- Chen, H., Karion, A., Rella, C. W., Winderlich, J., Gerbig, C., Filges, A., et al. (2013). Accurate measurements of carbon monoxide in humid air using the cavity ring-down spectroscopy (CRDS) technique. *Atmospheric Measurement Techniques*, 6(4), 1031–1040. <https://doi.org/10.5194/amt-6-1031-2013>
- Davis, K. J., Browell, E. V., Feng, S., Lauvaux, T., Obland, M. D., Pal, S., et al. (2021). The atmospheric carbon and transport (ACT)-America Mission. *Bulletin of the American Meteorological Society*, 102, 1–52. <https://doi.org/10.1002/essoar.10505721.1>
- Davis, K. J., Obland, M. D., Lin, B., Lauvaux, T., O'dell, C., Meadows, B., et al. (2018). *ACT-America: L3 merged in situ atmospheric trace gases and flask data, eastern USA*. Oak Ridge, TN: ORNL DAAC. <https://doi.org/10.3334/ORN-LDAAC/1593>
- DiGangi, J. P., Choi, Y., Nowak, J. B., Halliday, H. S., Diskin, G. S., Feng, S., et al. (2021). Seasonal variability in local carbon dioxide combustion sources over the central and eastern US using airborne in-situ enhancement ratios. In review, *Earth and Space Science Open Archive*. <https://doi.org/10.1002/essoar.10505716.1>
- Duncan, B. N., Logan, J. A., Bey, I., Megretskaia, I. A., Yantosca, R. M., Novelli, P. C., et al. (2007). Global budget of CO, 1988–1997: Source estimates and validation with a global model. *Journal of Geophysical Research*, 112, D22301. <https://doi.org/10.1029/2007jd008459>
- EPA (2019). *Air pollutant emissions trends data*. Retrieved from <https://www.epa.gov/air-emissions-inventories/air-pollutant-emissions-trends-data>

- Fisher, J. A., Murray, L. T., Jones, D. B. A., & Deutscher, N. M. (2017). Improved method for linear carbon monoxide simulation and source attribution in atmospheric chemistry models illustrated using GEOS-Chem v9. *Geoscientific Model Development*, 10(11), 4129–4144. <https://doi.org/10.5194/gmd-10-4129-2017>
- Friedlingstein, P., Jones, M., O'Sullivan, M., Andrew, R., Hauck, J., Peters, G., et al. (2019). Global carbon budget 2019. *Earth System Science Data*, 11(4), 1783–1838. <https://doi.org/10.5194/essd-11-1783-2019>
- Fujita, E. M., Campbell, D. E., Zielinska, B., Chow, J. C., Lindhjem, C. E., DenBleyker, A., et al. (2012). Comparison of the MOVES2010a, MOBILE6.2, and EMFAC2007 mobile source emission models with on-road traffic tunnel and remote sensing measurements. *Journal of the Air & Waste Management Association*, 62(10), 1134–1149. <https://doi.org/10.1080/10962247.2012.699016>
- Gaubert, B., Worden, H. M., Arellano, A. F. J., Emmons, L. K., Tilmes, S., Barré, J., et al. (2017). Chemical feedback from decreasing carbon monoxide emissions. *Geophysical Research Letters*, 44(19), 9985–9995. <https://doi.org/10.1002/2017gl074987>
- Gvakharia, A., Kort, E. A., Smith, M. L., & Conley, S. (2018). Testing and evaluation of a new airborne system for continuous N<sub>2</sub>O, CO<sub>2</sub>, CO, and H<sub>2</sub>O measurements: The frequent calibration high-performance airborne observation system (FCHAOS). *Atmospheric Measurement Techniques*, 11(11), 6059–6074. <https://doi.org/10.5194/amt-11-6059-2018>
- Halliday, H. S., DiGangi, J. P., Choi, Y., Diskin, G. S., Pusede, S. E., Rana, M., et al. (2019). Using short-term CO/CO<sub>2</sub> ratios to assess air mass differences over the Korean peninsula during KORUS-AQ. *Journal of Geophysical Research: Atmospheres*, 124(20), 10951–10972. <https://doi.org/10.1029/2018jd029697>
- Hoesly, R. M., Smith, S. J., Feng, L., Klimont, Z., Janssens-Maenhout, G., Pitkanen, T., et al. (2018). Historical (1750–2014) anthropogenic emissions of reactive gases and aerosols from the community emission data system (CEDS). *Geoscientific Model Development*, 11, 369–408. <https://doi.org/10.5194/gmd-11-369-2018>
- Hudman, R. C., Murray, L. T., Jacob, D. J., Millet, D. B., Turqueti, S., Wu, S., et al. (2008). Biogenic versus anthropogenic sources of CO in the United States. *Geophysical Research Letters*, 35, L04801. <https://doi.org/10.1029/2007gl032393>
- Hu, L., Jacob, D. J., Liu, X., Zhang, Y., Zhang, L., Kim, P. S., et al. (2017). Global budget of tropospheric ozone: Evaluating recent model advances with satellite (OMI), aircraft (IAGOS), and ozonesonde observations. *Atmospheric Environment*, 167, 323–334. <https://doi.org/10.1016/j.atmosenv.2017.08.036>
- Hu, L., Millet, D. B., Baasandorj, M., Griffis, T. J., Turner, P., Helmig, D., et al. (2015). Isoprene emissions and impacts over an ecological transition region in the US Upper Midwest inferred from tall tower measurements. *Journal of Geophysical Research: Atmospheres*, 120(8), 3553–3571. <https://doi.org/10.1002/2014jd022732>
- Kim, S. Y., Millet, D. B., Hu, L., Mohr, M. J., Griffis, T. J., Wen, D., et al. (2013). Constraints on carbon monoxide emissions based on tall tower measurements in the U.S. upper Midwest. *Environmental Science & Technology*, 47(15), 8316–8324. <https://doi.org/10.1021/es4009486>
- Koster, R. D., Darmenov, A. S., & da Silva, A. M. (2015). The Quick Fire Emissions Dataset (QFED): Documentation of Versions 2.1, 2.2 and 2.4. Volume 38; *Technical Report Series on Global Modeling and Data Assimilation*. Retrieved from <https://gmao.gsfc.nasa.gov/pubs/docs/Darmenov796.pdf>
- Lucchesi, R. (2013). File specification for GEOS-5 FP. GMAO Office Note No. 4 (Version 1.0). Retrieved from <https://gmao.gsfc.nasa.gov/pubs/docs/Lucchesi617.pdf>
- Millet, D. B., Conley, S. A., Gvakharia, A., Kort, E. A., Plant, G., Smith, M. L., & Yu, X. (2019). Airborne measurements from the GEM study. Retrieved from Data Repository for the University of Minnesota. <https://doi.org/10.13020/f50r-zh70>
- Müller, J. F., Stavrou, T., Bauwens, M., George, M., Hurtmans, D., Coheur, P. F., et al. (2018). Top-down CO emissions based on IASI observations and hemispheric constraints on OH Levels. *Geophysical Research Letters*, 45(3), 1621–1629. <https://doi.org/10.1002/2017gl076697>
- Nathan, B. J., Lauvaux, T., Turnbull, J. C., Richardson, S. J., Miles, N. L., & Gurney, K. R. (2018). Source sector attribution of CO<sub>2</sub> emissions using an urban CO/CO<sub>2</sub> Bayesian inversion system. *Journal of Geophysical Research: Atmospheres*, 123, 13611–13621. <https://doi.org/10.1029/2018jd029231>
- National Emissions Inventory Collaborative (NEIC) (2019). 2016beta emissions modeling platform. Retrieved from <http://views.cira.colostate.edu/wiki/wiki/10197>
- National Emissions Inventory (NEI) (2014). Air emissions inventories. Retrieved from [https://edap.epa.gov/public/extensions/nei\\_report\\_2014/dashboard.html#sector-db](https://edap.epa.gov/public/extensions/nei_report_2014/dashboard.html#sector-db)
- Nopmongcol, U., Grant, J., Knipping, E., Alexander, M., Schurhoff, R., Young, D., et al. (2017). Air quality impacts of electrifying vehicles and equipment across the United States. *Environmental Science & Technology*, 51(5), 2830–2837. <https://doi.org/10.1021/acs.est.6b04868>
- Parrish, D. D. (2006). Critical evaluation of US on-road vehicle emission inventories. *Atmospheric Environment*, 40(13), 2288–2300. <https://doi.org/10.1016/j.atmosenv.2005.11.033>
- Plant, G., Kort, E. A., Floerchinger, C., Gvakharia, A., Vimont, L., & Sweeney, C. (2019). Large fugitive methane emissions from urban centers along the U.S. East Coast. *Geophysical Research Letters*, 46, 8500–8507. <https://doi.org/10.1029/2019GL082635>
- Salmon, O. E., Shepson, P. B., Ren, X., He, H., Hall, D. L., Dickerson, R. R., et al. (2018). Top-down estimates of NO<sub>x</sub> and CO emissions from Washington, DC-Baltimore during the WINTER campaign. *Journal of Geophysical Research: Atmospheres*, 123(14), 7705–7724. <https://doi.org/10.1029/2018jd028539>
- Shindell, D. T., Faluvegi, G., Koch, D. M., Schmidt, G. A., Unger, N., & Bauer, S. E. (2009). Improved attribution of climate forcing to emissions. *Science*, 326(5953), 716–718. <https://doi.org/10.1126/science.1174760>
- Super, I., Denier van der Gon, H. A. C., Visschedijk, A. J. H., Moerman, M. M., Chen, H., Van der Molen, M. K., & Peters, W. (2017). Interpreting continuous in-situ observations of carbon dioxide and carbon monoxide in the urban port area of Rotterdam. *Atmospheric Pollution Research*, 8(1), 174–187. <https://doi.org/10.1016/j.apr.2016.08.008>
- Wei, Y., Shrestha, R., Pal, S., Gerken, T., McNelis, J., Singh, D., et al. (2021). The ACT-America datasets: Description, management and delivery. In press, *Earth and Space Science*. <https://doi.org/10.1002/essoar.10505692.1>
- Winkler, S. L., Anderson, J. E., Garza, L., Ruona, W. C., Vogt, R., & Wallington, T. J. (2018). Vehicle criteria pollutant (PM, NO<sub>x</sub>, CO, HCs) emissions: How low should we go? *npj Climate and Atmospheric Science*, 1(1), 1–5. <https://doi.org/10.1038/s41612-018-0037-5>
- Wofsy, S. C., Afshar, S., Allen, H. M., Apel, E. C., Asher, E. C., Barletta, B., et al. (2018). Atom: Merged atmospheric chemistry, trace gases, and aerosols. Oak Ridge, TN: ORNL DAAC. <https://doi.org/10.3334/ORNLDAAC/1581>
- Yu, X., Millet, D. B., Wells, K. C., Griffis, T. J., Chen, X., Baker, J. M., et al. (2020). Top-down constraints on methane point source emissions from animal agriculture and waste based on new airborne measurements in the US Upper Midwest. *Journal of Geophysical Research: Biogeosciences*, 125(1), e2019JG005429. <https://doi.org/10.1029/2019JG005429>
- Yu, X., Millet, D. B., Wells, K. C., Henze, D. K., Cao, H., Griffis, T. J., et al. (2021). Aircraft-based inversions quantify the importance of wetlands and livestock for Upper Midwest methane emissions. *Atmospheric Chemistry and Physics*, 21(2), 951–971. <https://doi.org/10.5194/acp-21-951-2021>